Three-Dimensional Characterization of Cryogenic Target Ice Layers Using Multiple Shadowgraph Views

Introduction

The 60-beam, 30-kJ OMEGA Laser System[1] studies the laser-driven direct-drive ignition approach to inertial confinement fusion (ICF) in which many individual high-power laser beams directly illuminate a spherical target to create a spherically symmetric implosion. Current designs for high-gain ICF targets include a layer of condensed hydrogen fuel that adheres to the inner surface of a thin spherical shell ablator. Laser energy delivered to the target ablates its outer surface and the ablation pressure drives the fuel layer inward, compressing both it and the gaseous fuel at the target's center. The drive pressure is varied in time such that the fuel density is compressed by a factor of as much as 4000 while remaining relatively cold. However, shock waves resulting from the drive-pressure variations, along with compressive work, heat the gaseous core "hot spot" to the high temperatures needed to initiate burning the fuel.

"Hot-spot" ignition is a common feature of all standard ignition experiments. This requires spherically symmetric implosions to limit the effects of hydrodynamic instabilities that can reduce fusion yield or prevent ignition by causing cold fuel to mix into the hot spot or target breakup. Asymmetry-induced hydrodynamics reduce the performance of most ICF targets well below that predicted by 1-D modeling.[2] The symmetry requirement imposes strong constraints on the uniformity of the laser illumination and on the sphericity of the target.[3] LLE has made great strides in reducing illumination asymmetries[2] due to drive imbalance between different beams and laser imprint. Efforts are also under way at LLE to reduce the asymmetries inherent in the target ice layer.[4]

The quality of a fuel–ice layer depends on the method used to form it. Extremely slow cooling (~1 mK/min) is required to avoid the formation of multiple crystals of different orientations.[5] Volumetric heating, in the form of infrared heating,[6] improves the sphericity of ice layers by driving ice mass from thicker sections of the layer to thinner areas via vapor pressure and sublimation. Ice surfaces in OMEGA cryogenic targets are beginning to approach the 1-μm root-mean-square (rms) deviation requirement[3] for successful ignition on the NIF.[7]

The degrading effect of surface roughness on implosion performance depends on the perturbation's mode number, which is the ratio of the capsule's circumference to the wavelength of the perturbation. The surface roughness is characterized in terms of a mode spectrum analogous to Fourier analysis. Since the target geometry is spherical, however, spherical harmonics

$$Y_{\ell m}(\theta,\phi) \equiv \left[\frac{(2\ell+1)}{4\pi}\frac{(\ell-m)!}{(\ell+m)!}\right]^{1/2} P_{\ell m}(\cos\theta)e^{im\phi}$$

$$-\ell \le m \le \ell, \tag{1}$$

where $P_{\ell m}$ are the associated Legendre functions, form the base functions used for the mode spectrum. Accurate surface characterization of ice layers requires reliable measurement of the layer's surface with submicron resolution at many points distributed over the surface of a target. Hydrodynamic codes then calculate capsule implosion performance using the measured surface mode power spectrum. The benchmarking of calculated target performance with experimental results is essential for designing ignition-scale targets and specifying their allowable surface roughness with confidence.

This article describes the optical backlit shadowgraphic characterization of cryogenic target ice layers with submicron resolution at LLE. A novel feature of this work is the ability to image the target from many different views. The analyses of multiple images of the target from different views are combined to construct a 3-D representation of the ice layer and an ice-roughness power spectrum in terms of spherical harmonics. There are many advantages to using a full 3-D representation over a single view or even over a few orthogonal views.

- The probability of missing significant local defects in the ice layer is greatly reduced.
- A 2-D surface-roughness spectrum suitable for input into a hydrodynamic code can be directly calculated. A single view provides only a 1-D Fourier roughness spectrum.

- Future detailed comparison of experimental implosions and 3-D simulations will require full surface ice characterization.

- Discrimination is possible between bumps/divots and ridges/troughs that could appear similar in a single view.

- Discrimination is possible between some outer-surface perturbation effects on the bright ring and actual ice layer defects.

Shadowgraphic Characterization of Ice Layers (p. 170) briefly describes the principles and equipment used to record a cryogenic target shadowgraph at LLE and is followed by details of the analysis of an individual shadowgraph in **Analysis of Individual Shadowgraphs** (p. 171). The 3-D ice layer reconstruction and determination of the global surface roughness power spectrum from multiple target views are reported in **Three-Dimensional Ice Layer Reconstruction Using Multiple Shadowgraph Views** (p. 175).

Shadowgraphic Characterization of Ice Layers

Optical backlit shadowgraphy is a primary diagnostic for ICF target ice layer roughness measurements.[6,8–12] A shadowgraph records the image of light rays passing through a backlit target. The rays are reflected and refracted at the shell wall and ice layer surfaces; some rays are focused into characteristic rings. Ray-trace modeling has identified specific reflections/refractions responsible for the brightest rings (see Fig. 104.1). The most prominent or "bright" ring is the result of total internal reflection off the inner solid–vapor interface of the ice layer. The position of the bright ring in the shadowgraph is directly correlated with the position of the inner surface of the ice layer and thus allows characterization of the nonuniformity of the inner surface.

A high-magnification, high-fidelity backlit optical shadowgraphy system (Fig. 104.2) is used to diagnose the ice layer quality while a target is in one of two characterization stations. A 612-nm red LED provides backlighting, and a 0.1- to 30-ms pulse drives the LED that is coupled to a 450-μm multimode fiber used to illuminate (~*f*/23) the target. An *f*/6 imaging optic magnifies the target on a Dalsa CCD camera (12 bit, 1024 × 1024) (Ref. 13) such that the camera typically images about 1.2 μm per pixel. The camera is triggered by and integrates over the same pulse that drives the LED.

A sample shadowgraph of a LLE cryogenic target suspended from a beryllium "c mount" by four threads of spider silk (a polymerized scleroprotein)[14] is shown in Fig. 104.3. The strong, unbroken bright ring and mostly featureless central spot are indicative of the high quality of this ice layer. Two inner rings are also clearly visible.

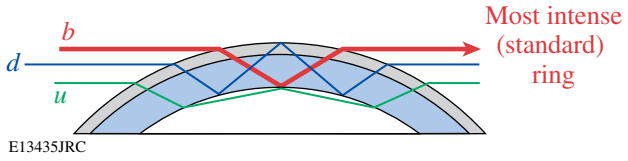

Figure 104.1
Ray-trace modeling of a cryogenic target has identified the sources of the most intense rings. The bright ring *b* is by far the most intense.

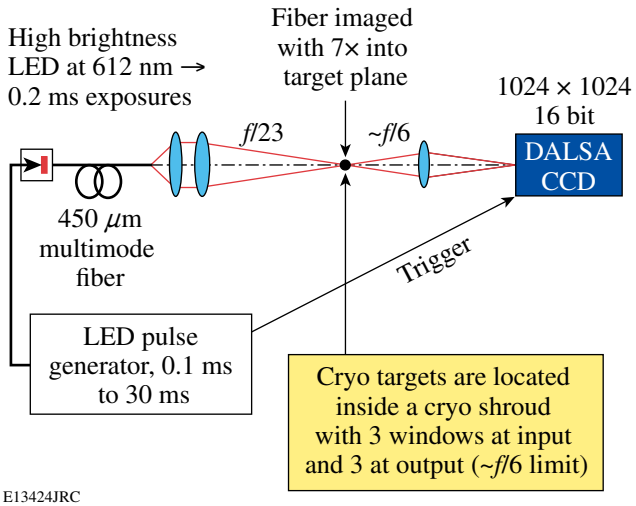

Figure 104.2
The LLE cryogenic target characterization stations are based on a diffuse *f*/23 source and *f*/6 imaging optics.

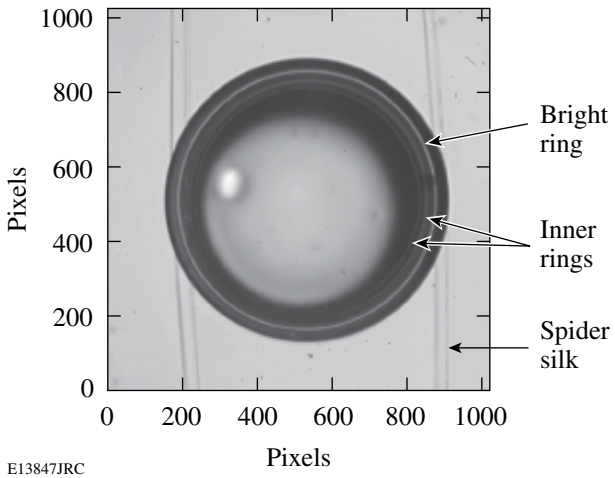

Figure 104.3
Shadowgraph of a cryogenic target in a logarithmic scale. The fainter inner rings are clearly visible in the image.

Analysis of Individual Shadowgraphs

The shadowgraph analysis is performed by a MATLAB[15] routine, *viewcryo*, that uses several automated steps that include:

1. Rough estimation of the target radius and center
2. Unwrapping the image in polar coordinates
3. Identification of spider webs
4. Refinement of the target edge and center estimate
5. Repetition of steps 2–4 until the target center coordinates change by less than ~0.005 μm
6. Identification of the bright ring using Gaussian fitting routines
7. Determination of the ice layer thickness
8. Fourier analysis of the ice layer

Details regarding each step are given below.

1. Rough Estimation of the Target Radius and Center

The target image is roughly centered in the CCD image by design and alignment. A first rough estimate of the target center location is obtained from horizontal and vertical lineouts (e.g., Fig. 104.4) averaged over several (~10) pixels. Taking the midpoints between the clearly visible target edges yields target center coordinates that are typically within one pixel of the more accurate center-finding routines discussed below.

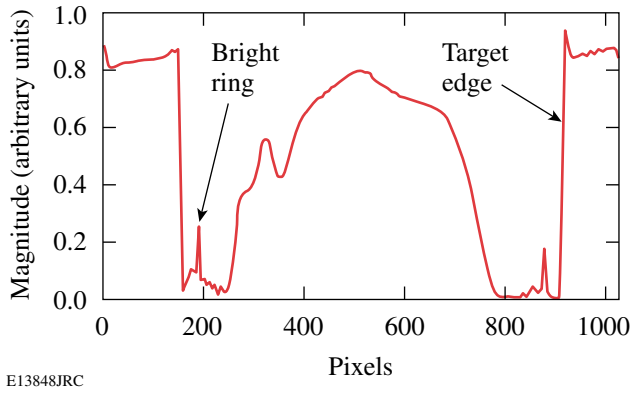

Figure 104.4
Horizontal lineout through the center of the image shown in Fig. 104.3 and averaged over ~10 pixels.

2. Unwrapping the Image in Polar Coordinates

With an estimate of the target center, the image can be mapped to (θ,r) polar coordinates by determining the image intensity along radial lines at fixed angular intervals. A super-Gaussian interpolation function unwraps the target image to an evenly spaced grid in (θ,r), and the interpolation function has separate Gaussian widths optimized for the angular and radial dimensions.[16] The separation of interpolation parameters allows subpixel resolution in the radial direction necessary to determine the roughness of the rather smooth outer-target surface and inner-ice layer. Pixel smoothing in the angular dimension is possible while allowing resolution of high mode numbers in the Fourier analysis of the target surfaces. Figure 104.5 shows the unwrapped image of the target edge using the initial rough estimate of the target center for the shadowgraph shown in Fig. 104.3. The unwrapped target edge shows a large $n = 1$ Fourier component, indicating an offset in the actual target center from the initial estimate. This $n = 1$ component is used below to correct the target center coordinates and, after several iterations, the center coordinates converge to a ≤0.005-μm variation from iteration to iteration.

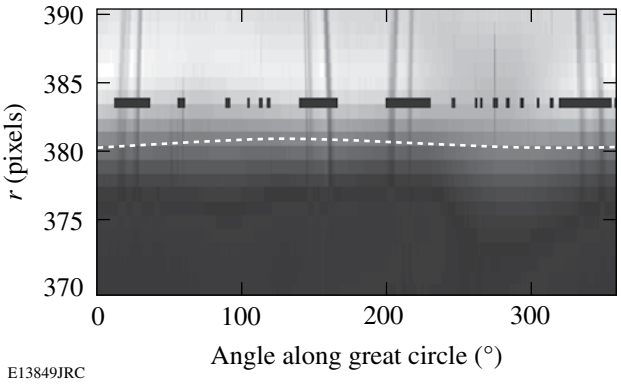

Figure 104.5
Close-up of the step in intensity at the target edge for the initial unwrapping of the shadowgraph shown in Fig. 104.3. The black bars indicate gaps where the edge data is *not* used to determine the target center due to the influence of spider webs and other image features outside the target. The white dotted line shows the position of the target edge (midpoint of the intensity step). The $n = 1$ component in the target edge results from an offset in the estimated target center that has not yet been removed.

3. Identification of Spider Webs

The four spider webs used to support the cryogenic targets appear in every shadowgraphic image of the target. Absorption/reflection/diffraction of light by the webs distorts the CCD image of the target's outer surface where the web images cross. These corrupted portions of the outer edge images are not used in the target-edge and center-finding routines discussed below.

The *viewcryo* code identifies where the web traces intersect the target edge by examining the region of the unwrapped image just outside the edge and isolating sections where pixel values differ significantly from a local median value. The local median is calculated for a section broad enough that it is not

located on a web. The results of the spider web identification for an initial image unwrapping are shown in Fig. 104.5.

4. Refinement of the Target Edge and Center Estimates

The target center position in the image is accurately determined by removing the $n = 1$ Fourier component of the target edge measurements in the unwrapped image. This component corresponds to a linear offset in the determination of the target center. The target edge is determined by examining the radial variation in intensity at each angular position in the unwrapped image (e.g., the data points in Fig. 104.6). While the edge corresponds to a step in intensity, no single smooth-step function (e.g., an error function) would be a good match to the data mainly because of the "overshoot" at the top of the step. A least-squares fit of the data to a set of many smooth step functions produces a good fit to the features of the measured step along with essentially flat regions on either side of the step as shown by the solid line in Fig. 104.6. The step function set consists of many (~35) error-function traces of varying widths and centers covering a range appropriate for the target edge. Negative fitting coefficients enable the fit to replicate the "overshoot" and other nonmonotonic features. Least-squares fitting via a matrix inversion results in a very fast fit. The target-edge position is defined as the radial point where the fit height is halfway between the heights of the flat regions on either side of the edge step. The radial location of this halfway point can be resolved to 0.1 pixel as is shown in **Shadowgraph Resolution** (p. 174). The data points in Fig. 104.7 show the angular variation in target's outer-edge position along a great circle.

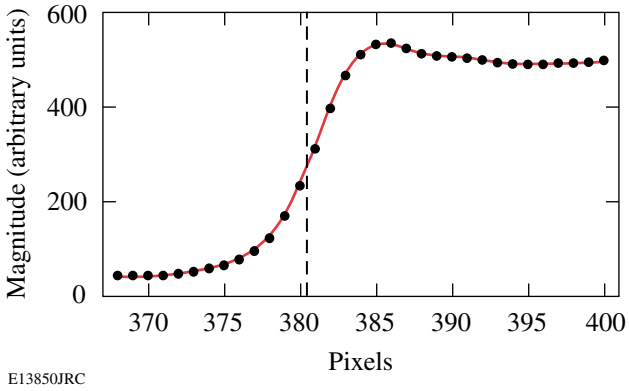

Figure 104.6
Radial variation of intensity at a specific angular position in an unwrapped image (circles) and the result of a least-squares fit to a set of error functions (solid line). The edge location (dashed line) is taken to be the radial point where the fit height is half way between the heights of the flat regions on either side of the edge step.

The variation in target-edge position with angular position is decomposed into its low-mode number (up to $n = 6$) Fourier components to remove the $n = 1$ component. These modes are sufficient to determine the large amplitude variations in the target-edge position as shown by the reconstruction (solid line) in Fig. 104.7. As mentioned previously, angular regions previously identified by the spider web finding routine are excluded from the Fourier decomposition. The routine also automatically excludes outliers from the target center finding Fourier decomposition. Outliers are identified by their deviation from the Fourier reconstruction as compared to the standard deviation and determined in terms of deviation in fitted step height, width, and radial position. The Fourier decomposition is performed iteratively with outliers excluded to ensure a self-consistent result is found. Outliers automatically identified in this way typically result from additional corruption of the edge image by spider webs, dust, and other image defects.

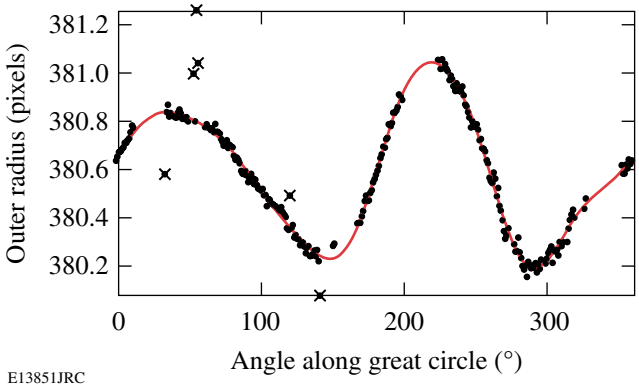

Figure 104.7
Angular variation in target edge radius as determined by the analysis of the image in Fig. 104.3 (dots) along with the fit to low mode number (up to $n = 6$) Fourier components (line). The x's indicate data points automatically excluded from the Fourier decomposition as outliers. The large angular gaps in the data indicate regions excluded from the decomposition by the spider web finding routine.

The estimated target center position is now adjusted to eliminate the $n = 1$ Fourier component of the target's outer edge found by the decomposition that corresponds to a linear target offset. The unwrapping, spider web finding, and target edge determination are repeated iteratively until the $n = 1$ target offset is reduced to some arbitrarily small number, typically $\leq 0.005\ \mu$m.

5. Identification of the Bright Ring and Determination of the Ice Surface Radius

The bright ring location is identified by fitting a Gaussian peak to the radial intensity profile in the vicinity of the ring at each angular position of the unwrapped image (Fig. 104.8). The data points in Fig. 104.9 show the angular variation in bright position around the target. The bright ring intensity is well fit by a Gaussian peak, provided the image is focused on that ring. Ray-trace modeling of a typical cryogenic target using the *PEGASUS* code[17] has not only identified the sources of the prominent shadowgraph rings, but also how the ring positions vary with the target parameters such as shell outer radius, shell thickness, D_2 ice thickness, shell index of refraction, and the D_2 index of refraction. The *PEGASUS* code is 2-D and assumes spherical symmetry in the target. A linearized formula derived from this modeling is used to determine the inner-ice-surface radius from the position of the bright ring for given target parameters. Efforts are currently under way to extend the ray-trace modeling to 3-D and to explore the effects of ice-surface roughness on the bright ring in detail.

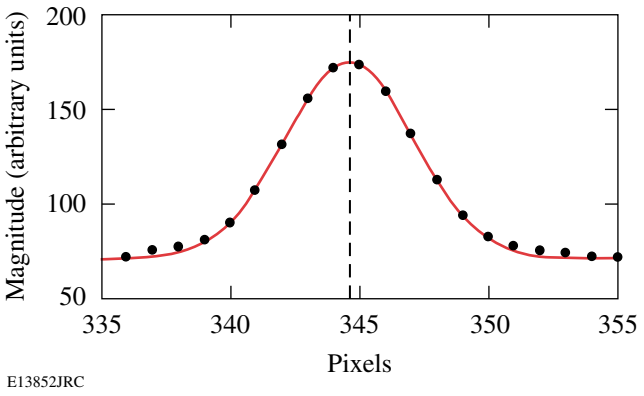

Figure 104.8
The radial location of the bright ring (dashed line) is determined by the center of a Gaussian fit (solid line) to the radial variation in intensity across the ring (dots).

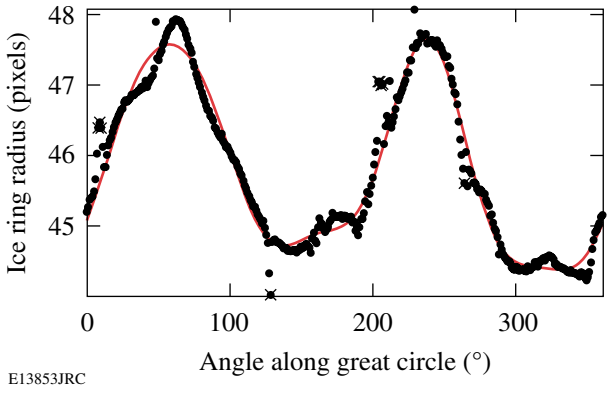

Figure 104.9
Typical angular variation in bright ring radius as determined by the analysis (dots) along with the fit to low-mode number (up to $n = 9$) Fourier components (line). The x's indicate data points automatically excluded from the Fourier decomposition as outliers.

6. Fourier Analysis of the Ice Layer

The roughness and asymmetry of the inner-ice surface can degrade the performance of a cryogenic target on implosion. The Fourier power spectrum of the ice layer roughness around a great circle of the target is calculated directly from the variation in ice layer thickness or inner-ice-surface position $R(\theta)$ as determined from the bright ring analysis. We use the convenient series

$$R(\theta) = a_0 + \sqrt{2}\sum_{n=1}^{\infty}\left[a_n\cos(n\theta) + b_n\sin(n\theta)\right](\mu\text{m}) \qquad (2)$$

for Fourier decomposition. The $\sqrt{2}$ factor results in a total variance and a 1-D Fourier power spectrum of

$$\sigma^2_{\text{rms}} = \frac{1}{2\pi}\int_{-\pi}^{\pi}\left[R(\theta) - \overline{R}\right] = \sum_{n=1}^{\infty} P_n \ (\mu\text{m}) \qquad (3)$$

and

$$P_n = a_n^2 + b_n^2 \ (\mu\text{m}^2), \qquad (4)$$

respectively. The 1-D power spectrum of the cryogenic ice layer from the shadowgraph of Fig. 104.3 is shown in Fig. 104.10. The total 1-D rms of this layer is 1.36 μm. The majority of this roughness is due to the large $n = 2$ component. The total 1-D rms of all modes except $n = 2$ is less than 0.2 μm.

The 1-D Fourier power spectrum derived from a great circle ice layer measurement is a useful gauge of target quality. However, a computer simulation of implosions including instability growth and implosion performance requires a true spherical harmonic surface representation of the ice layer roughness. In **Three-Dimensional Ice Layer Reconstruction Using Multiple Shadowgraph Views** (p. 175), we will discuss using multiple shadowgraphs of different views to determine the surface asymmetry and ice roughness in terms of spherical harmonics.

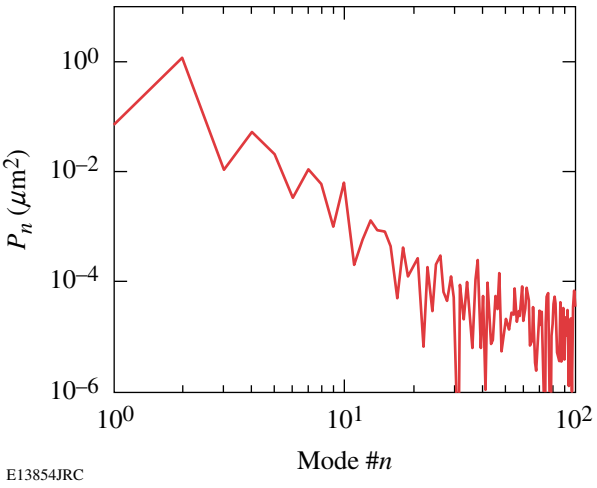

Figure 104.10
Fourier power spectrum of the ice layer from analysis of the shadowgraph shown in Fig. 104.3.

The modal analysis can be complicated by gaps in the bright ring due to ice or other defects. Direct Fourier decomposition of only the good points between the gaps is limited to relatively low mode numbers whose exact limit depends on the size of the gaps. This method prevents estimation of the high-mode ice roughness and aliases the high-mode information into errors in the low-mode determinations. Interpolation is used to bridge the gaps before the Fourier analysis. As the interpolation over small gaps preserves low-mode structure, the error due to the interpolation tends to be concentrated in higher modes, typically increasing the estimate of the higher-mode ice roughness along with an accurate determination of the low-mode ice asymmetries despite the gaps. Ice surface defects that cause gaps should ideally be included in the surface roughness analysis; however, determining the true nature of the defects is difficult. Efforts are under way to identify ice defects using nonbright ring rays from multiple views.[18]

7. Shadowgraph Resolution

The resolution of the shadowgraphic analysis has been examined using a sapphire sphere surrogate target for the outer-edge determination and a cryogenic target with a melted layer for the bright ring measurements. Figure 104.11 shows the scatter in outer-edge analysis from several images of a sapphire sphere at the same rotated position scaled to the nominal outer radius of 395 μm. Small vibrations varied the target's position by a few microns between the various images ensuring that the edge crossed the CCD pixel array pattern (~1 pixel/μm) at different locations in each image. Both large- and small-scale features in the edge analysis are highly repeatable. The standard deviation between the analyses is of the order 0.01 μm at all angles. The peak-to-peak variation in edge radius is comparable to that measured for the sphere by an atomic force microscope[19] along different great circles.

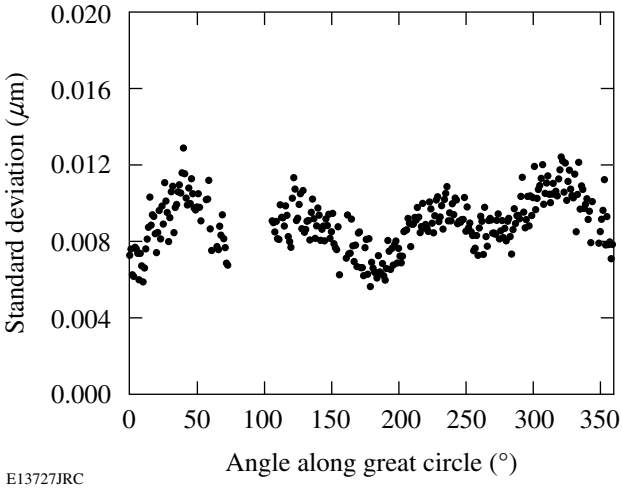

Figure 104.11
Standard deviation between outer-edge measurements of 17 different shadowgraphs viewing a sapphire sphere at slightly different positions due to vibrations of the order of a pixel. The target-mounting stalk is at 90° and causes the gap in the data at that angle.

The resolution of the bright ring measurements has been studied by analyzing the bright ring from targets whose ice layer has partially or fully melted (for an example see Fig. 104.12). In both cases, the bright ring from the very smooth liquid hydrogen surface shows an rms roughness of about 0.1 pixel (~0.12 μm).

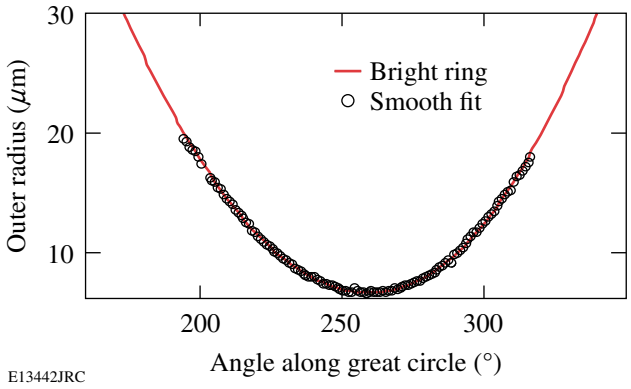

Figure 104.12
Bright ring measurements for the liquid portion of a partially melted target show a 0.1-pixel (~12-μm) rms roughness versus a smooth fit using Fourier modes 0, 1, and 2.

An error analysis of the shadowgraphic target characterization using a fully atomic-force-microscope–characterized sapphire sphere surrogate target and precision planar pattern targets is under way and will be reported in a future publication.

Three-Dimensional Ice Layer Reconstruction Using Multiple Shadowgraph Views

An important feature of LLE's cryogenic target shadowgraph system is the use of multiple views of the target to fully characterize the ice layer. Multiple views allow a far more complete layer characterization than is possible from a single view. In fact, even with three mutually orthogonal views, it can be shown that there is only a small chance of detecting many local ice defects.[19] The targets are rotated in the cryogenic target characterization stations, providing a large number of different views for a single camera. The maximum number of views is limited only by the rotation stepper motor step size of a few tenths of a degree.

Shadowgraphs are typically recorded at 15° intervals, producing a total of 48 independent views between two cameras in each station. It takes less than a minute to rotate the target to each image view. After an image is taken, the target is rotated back to its "home" position for a short rest. This procedure prevents significant changes in the ice layer due to the changing target position with respect to the geometry of the isotherms in the layering sphere. The time constant for an ice layer to change because of target rotation is of the order of 15 to 25 min, much longer than the typical time required to obtain an image at any view using this procedure. Figure 104.13 shows a target inner-ice surface reconstructed from 48 separate views. Very different low-mode asymmetries are observed for any given great circle. For this data set, the ice surface 1-D rms roughness of the individual great circle observations varies from 0.72 to 2.9 μm with an average value of 1.7 μm.

The two cameras in each characterization station have approximately orthogonal views. One camera views the target center from an angle of 26.56° above the equator. The second camera is located 109.96° azimuthally from the first and views from 12.72° above the equator. These view angles are determined by the locations of the layering sphere windows that are aligned with the OMEGA target chamber viewing ports used to center the target at shot time. Unfortunately, these views are not optimum for target characterization. An off-the-equator viewing angle always results in regions surrounding the rotation poles that cannot be observed. These unviewable "polar caps" are apparent in Fig. 104.13.

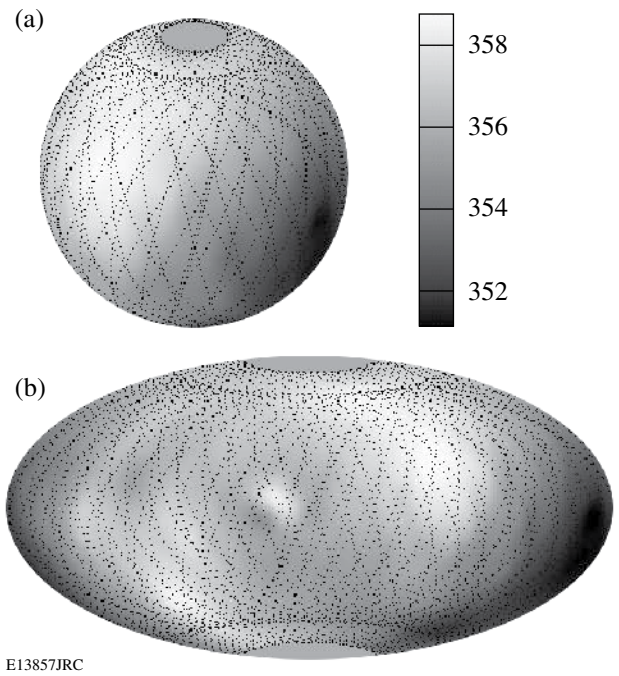

Figure 104.13
Three-dimensional representation of a cryogenic inner-ice surface (μm) displayed (a) on a spherical surface and (b) using the Aitoff projection. These displays are constructed by interpolating all the individual data from the many great circle observations to an evenly spaced (θ,ϕ) surface grid. The dotted lines show the location of the actual great circles observed in the individual shadowgraphs. The polar caps not crossed by the great circle observations are clearly visible. Typical surface structures are much more apparent in false color than in the gray scale representation required for publication.

As mentioned earlier, computer modeling of a spherical implosion including instability growth requires an ice roughness spectrum described in terms of spherical harmonics basis functions $Y_{\ell m}(\theta,\phi)$ on the ice surface.

$$R(\theta,\phi) = \sum_{\ell=0}^{\infty} \sum_{m=-\ell}^{\ell} A_{\ell m} Y_{\ell m}(\theta,\phi) \ (\mu m). \tag{5}$$

This description gives a power spectrum and total surface variance of

$$P_\ell = \frac{1}{4\pi} \sum_{m=-\ell}^{\ell} \left| A_{\ell m} \right|^2 \ \left(\mu \mathrm{m}^2\right) \tag{6}$$

and

$$\sigma_{\mathrm{rms}}^2 = \sum_{\ell=1}^{\infty} P_\ell \left(\mu \mathrm{m}^2\right), \tag{7}$$

respectively. The Legendre mode spectrum P_ℓ represents a sum over all azimuthal modes m. Multiple views allow the inner-ice surface to be directly fit to the $Y_{\ell m}(\theta,\phi)$'s. This fit has an upper limit on the mode number ℓ_{max} determined by the largest space between sampled points on the surface. For typical LLE targets, the largest gap in the surface data occurs at the unviewable polar cap of the target. The many smaller surface gaps between great circle measurements, noise in the data, and uneven surface weighting (sections crossed by several great circles are more heavily weighted) also reduce the maximum mode number that can be reliably fit. These effects typically limit the direct surface fit to mode numbers to about $\ell_{max} = 8$ to 10. The exact limit varies with each data set.

The results of a direct $Y_{\ell m}(\theta,\phi)$ fit are shown in Figs. 104.14 and 104.15. The surface reconstruction in Fig. 104.14 based on the low-mode number fit is a very good match to the data shown in Fig. 104.13. The Legendre power spectrum P_ℓ corresponding to this fit is displayed in Fig. 104.15.

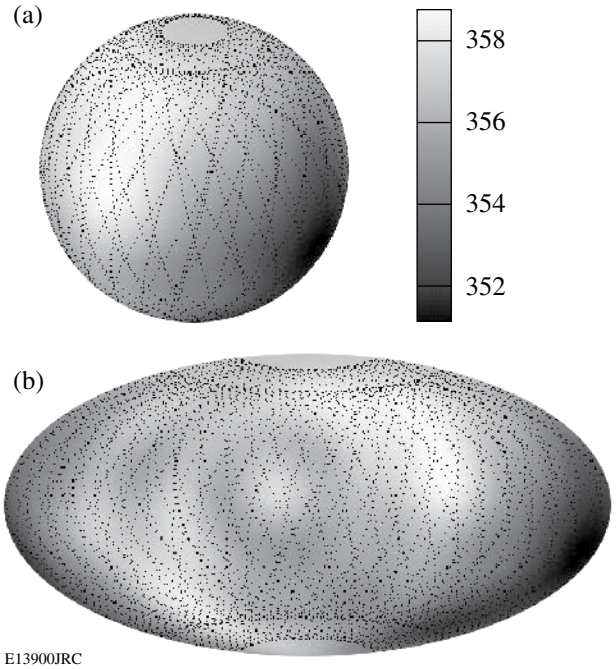

Figure 104.14
Three-dimensional reconstruction of a cryogenic inner-ice surface (μm) based on a direct $Y_{\ell m}(\theta,\phi)$ fit to the measured data. A comparison with Fig. 104.13 shows that the low-mode features are well matched by the fit. Although the actual great circle data are used in the fitting, the results are mapped to an evenly spaced (θ,ϕ) surface grid using the $Y_{\ell m}$ coefficients for better display.

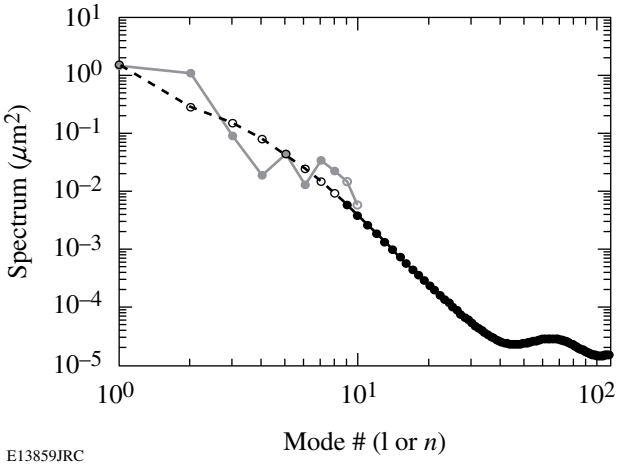

Figure 104.15
Legendre-mode power spectrum P_ℓ of the ice surface. The gray data correspond to the low-mode-number direct fit. The black data are the result from mapping the average Fourier mode spectrum (see Fig. 104.16) of the many great circles.

Mode numbers higher than ℓ_{max} cannot be directly fit, but can be inferred from the Fourier power spectra of the many great circles observed. If one assumes that the surface perturbations are randomly distributed, the great circle 1-D Fourier-mode power spectrum averaged over many great circles can be mapped[20] to an equivalent Legendre-mode power spectrum. The assumption of randomly distributed perturbations limits the applicability of the mapping to higher mode numbers. Mode numbers up to about $\ell_{max} = 8$ to 10 are directly fit to spherical harmonics, while higher mode numbers are determined by this mapping of the average Fourier power spectrum. Figure 104.16 shows the Fourier-mode spectrum $\langle P_n \rangle$ averaged over the many great circle views. $\langle P_n \rangle$ is first smoothed, then mapped to the equivalent high-mode-number Legendre-mode power spectrum P_ℓ shown in Fig. 104.15. The smoothing improves the behavior of the mapping.

The recently updated[21] NIF indirect-drive specification for ice surface roughness is also plotted in Fig. 104.16. For this target, the ice layer roughness is well below the NIF specification for most mode numbers. Only modes $n = 1$ and 2 significantly exceed the specification. The bulk of the surface-roughness rms of 1.7 μm is in these two modes. Efforts are currently under way at LLE to understand and correct the sources of the low-mode asymmetries in the layering-sphere isotherms.[4]

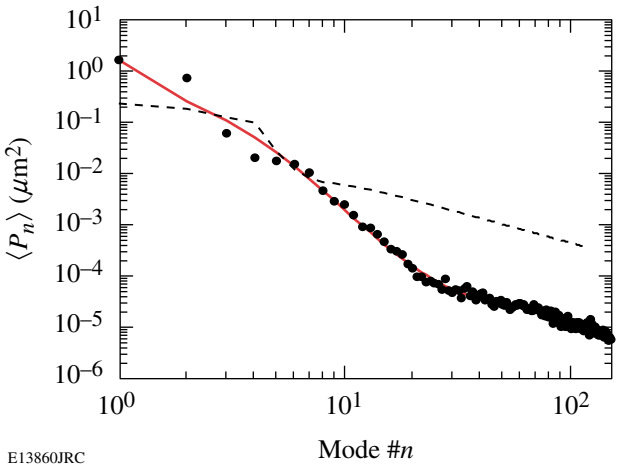

Figure 104.16
Average Fourier-mode spectrum $\langle P_n \rangle$ for the many great circle measurements of the ice surface used in the 3-D layer characterization. The dots are the actual average power for each mode number. The solid line is a smooth fit to the data used for the mapping to a Legendre-mode spectrum. The dashed line shows the recently updated NIF specification for indirect-drive ice layer roughness.

Summary

Analysis of the bright ring in backlit optical shadowgraphs of cryogenic targets is the primary diagnostic for ice layer quality at LLE. The bright ring radius is typically measured with a resolution of about 0.12 μm and is directly correlated to the position of the inner-ice surface. Two approximately orthogonal cameras and *in-situ* rotation of the target produce multiple shadowgraphs and, after analysis, the inner-ice surface radius for many different great circles on the target surface. A 3-D reconstruction of the inner-ice surface from these many views allows a direct fit of the surface roughness in terms of spherical harmonics for mode numbers up to ℓ_{max} = 8 to 10. The surface-roughness Legendre-mode spectrum for higher mode numbers is determined by mapping the 1-D Fourier-mode spectrum averaged over all of the great circles. The final Legendre-mode spectrum for the surface roughness is suitable for input to implosion modeling codes.

ACKNOWLEDGMENTS

This work was supported by the U.S. Department of Energy Office of Inertial Confinement Fusion under Cooperative Agreement No. DE-FC52-92SF19460, the University of Rochester, and the New York State Energy Research and Development Authority. The support of DOE does not constitute an endorsement by DOE of the views expressed in this article.

REFERENCES

1. T. R. Boehly, D. L. Brown, R. S. Craxton, R. L. Keck, J. P. Knauer, J. H. Kelly, T. J. Kessler, S. A. Kumpan, S. J. Loucks, S. A. Letzring, F. J. Marshall, R. L. McCrory, S. F. B. Morse, W. Seka, J. M. Soures, and C. P. Verdon, Opt. Commun. **133**, 495 (1997).
2. D. D. Meyerhofer, J. A. Delettrez, R. Epstein, V. Yu. Glebov, V. N. Goncharov, R. L. Keck, R. L. McCrory, P. W. McKenty, F. J. Marshall, P. B. Radha, S. P. Regan, S. Roberts, W. Seka, S. Skupsky, V. A. Smalyuk, C. Sorce, C. Stoeckl, J. M. Soures, R. P. J. Town, B. Yaakobi, J. D. Zuegel, J. Frenje, C. K. Li, R. D. Petrasso, D. G. Hicks, F. H. Séguin, K. Fletcher, S. Padalino, M. R. Freeman, N. Izumi, R. Lerche, T. W. Phillips, and T. C. Sangster, Phys. Plasmas **8**, 2251 (2001).
3. P. W. McKenty, V. N. Goncharov, R. P. J. Town, S. Skupsky, R. Betti, and R. L. McCrory, Phys. Plasmas **8**, 2315 (2001).
4. *LLE Review Quarterly Report* **99**, 160, Laboratory for Laser Energetics, University of Rochester, Rochester, NY, LLE Document No. DOE/SF/19460-555 (2004).
5. J. Sater *et al*., Fusion Technol. **35**, 229 (1999).
6. D. N. Bittner *et al*., Fusion Technol. **35**, 244 (1999).
7. W. J. Hogan, E. I. Moses, B. E. Warner, M. S. Sorem, and J. M. Soures, Nucl. Fusion **41**, 567 (2001).
8. J. K. Hoffer *et al*., Fusion Technol. **30**, 529 (1996).
9. J. D. Sheliak *et al*., Fusion Technol. **30**, 83 (1996).
10. B. J. Kozioziemski *et al*., in *Inertial Fusion Sciences and Applications 2003*, edited by B. A. Hammel *et al*. (American Nuclear Society, La Grange Park, IL, 2004), pp. 762–765.
11. J. A. Koch *et al*., Fusion Technol. **38**, 123 (2000).
12. J. A. Koch *et al*., Fusion Sci. Technol. **43**, 55 (2003).
13. DALSA, Waterloo, Ontario, Canada, N2V 2E9 (see http://www.dalsa.com).
14. M. J. Bonino, "Material Properties of Spider Silk," M.S. Thesis, University of Rochester, 2003.
15. G. J. Borse, *Numerical Methods with MATLAB:® A Resource for Scientists and Engineers* (PWS Publishing, Boston, 1997).
16. This algorithm was developed by one of the authors, A. Warrick, while on leave of absence at LLE.
17. S. Jin, *2002 Summer Research Program for High School Juniors at the University of Rochester's Laboratory for Laser Energetics*, Rochester, NY, LLE Report No. 329, LLE Document No. DOE/SF/19460-479 (2003).
18. R. B. Stephens *et al*., Fusion Sci. Technol. **45**, 210 (2004).
19. S. Pollaine and S. Hatchett, Nucl. Fusion **44**, 117 (2004).
20. J. D. Moody, Lawrence Livermore National Laboratory, private communication (2005).